SUPPORTING MATERIALS FOR:

Next Generation Pathology Detection of T cell-Antigen Presenting Cell Immune Synapses in Human Liver Allografts

Michelle A. Wood-Trageser, Drew Lesniak, Alessandro Gambella, Kayla Golnoski, Sandy Feng, John Bucuvalas, Alberto Sanchez-Fueyo, A. Jake Demetris

TABLE OF CONTENTS **PAGE NUMBER**

SUPPORTING TABLES

Supporting Table 1. Antibodies used for multiplex IHC

Primary Antibody				Secondary Antibody	Tertiary Detection		
Target (clone, RRID*)	**Catalog Information (RRID*)**	**Dilution**	**Incubation**		**Reagent**	**Dilution**	**Incubation at RT**
Staining Conditions on Ventana Discovery ULTRA							
CD3 (polyclonal)	Agilent/Dako[1] A045201-2 (RRID: AB_2335677)	1:200	37°C, 32 min	DISC. OmniMap Anti-RB HRP (RUO; Roche[3], 760-4311, RRID: AB_2811043)	DISC. Cy5 Kit (RUO; Roche, 760-238)	predilute	40 min
HLA-DPB1/ MHCII (clone EPR11226)	Abcam[2], ab157210 (RRID: AB_2827533)	1:250	RT, 4 hrs	DISC. OmniMap Anti-RB HRP	DISC. Red 610 Kit (RUO; Roche, 760-245)	predilute	32 min
CD8 (clone C8/144B)	Agilent/Dako M710301-2 (RRID: AB_2075537)	1:250[8]	RT, 6 hrs	DISC. OmniMap Anti-MS HRP (RUO; Roche, 760-4310, RRID: AB_2885182)	CF405L Tyramide Conjugate (Biotium[5], 92198)	predilute	32 min
		1:500[7]	37°C, 32 min	DISC. OmniMap Anti-MS HRP	DISC. DCC Kit (RUO; Roche,760-240)	predilute	12 min
CD45 (clone 2B11+PD7/26)	Agilent/Dako M070101-2 (RRID: AB_2314143)	1:500	37°C, 32 min	DISC. OmniMap Anti-MS HRP	DISC. Rhodamine 6G Kit (RUO; Roche, 760-244)	predilute	32 min
CD34 (clone QBEnd10)	Agilent/Dako M716501-2 (RRID: AB_2063006)	1:100	RT, 4 hours	DISC. OmniMap Anti-MS HRP	DISC. DCC Kit	predilute	32 min
Staining Conditions on LabVision Autostainer 360							
CD34 (clone QBEnd10)	Agilent/Dako M716501-2 (RRID: AB_2063006)	1:100	RT, 4 hours	Horse Anti-Mouse IgG Antibody, Biotinylated (BA-2000, Vector Laboratories[4], RRID:AB_2313581)	Qdot 605 (Q10101MP, Molecular Probes/Invitrogen[6])	1:50	30 min
CD45 (clone 2B11+PD7/26)	Agilent/Dako M070101-2 (RRID: AB_2314143)	1:500	RT, 2 hours	Horse Anti-Mouse IgG Antibody, Biotinylated	Qdot 705 (Q10161MP, Molecular Probes/Invitrogen)	1:250	30 min
HLA-DPB1/ MHCII (clone EPR11226)	Abcam, ab157210 (RRID: AB_2827533)	1:1000	RT, 2 hours	Goat anti-Rabbit IgG Antibody, Biotinylated (BA-1000, Vector Laboratories, RRID:AB_2313606)	Qdot 800 (Q10171MP, Molecular Probes/Invitrogen)	1:500	30 min
Manual Staining Conditions							

MAC387 (S100A9)	Abcam, ab22506 (RRID: AB_447111)	1:12,000	Overnight @4°C	Horse Anti-Mouse IgG Antibody, Biotinylated	Qdot 655 (Q10123MP, Molecular Probes/Invitrogen)	1:1000	30 min

*RRID = Research Resource Identifier, [1]Agilent/Dako, Santa Clara, CA; [2]Abcam, Waltham, MA; [3]Roche, Indianapolis, IN; [4]Vector Laboratories, Burlingame, CA; [5]Biotium, Fremont, CA; [6]Molecular Probes, Eugene, OR; [7]For detection of CD8 from Feng, Hepatology, 2021; [8]For detection of CD8 in SMAC/polarization panel.

Supporting Table 2. Subset of Nanostring Inflammatory Gene Panel

BTLA	CXCL9	HLA-DRA	KLRK1
CCL19	CXCR4	HLA-DRB3	LAG3
CD2	CXCR6	HLA-E	LCK
CD27	GBP2	HLA-G	MMP9
CD274	GNLY	HMMR	PDCD1
CD3D	GPNMB	ICAM1	PDCD1LG2
CD3E	GZMA	ICOS	PECAM1
CD3G	GZMB	IFNG	PIK3CD
CD40	GZMK	IFNGR1	PLA2G7
CD40LG	HAVCR2	IL2RB	PRF1
CD44	HLA-A	IRF1	PTPRC
CD6	HLA-B	IRF4	SH2D1A
CD74	HLA-C	IRF7	SH2D1B
CD80	HLA-DMA	IRF8	SOCS1
CD86	HLA-DMB	ITGA4	STAT1
CD8A	HLA-DPA1	ITGAM	TIGIT
CTLA4	HLA-DPB1	ITGB2	TNFRSF18
CTSS	HLA-DQA1	ITK	TNFRSF4
CX3CR1	HLA-DQB1	JAK2	TOP2A

SUPPORTING METHODS

A. Multiplex IHC using Ventana Discovery Ultra

Staining for CD34/CD45/CD3/MHCII/CD8 was conducted on selected FFPE slides from iWITH, iWITH-IN, and ARTEMIS. Slides were subjected to deparaffinization and antigen retrieval with Target Retrieval solution (pH 9.0; Agilent/Dako, S236784-2, Santa Clara, CA) for 40 mins at 93°C in a vegetable steamer. Slides were incubated with consecutive rounds of antibody staining with HRP-tagged secondary antibodies, DISC. OmniMap Anti-MS HRP RUO (Roche, 760-4310, Indianapolis, IN; RRID:AB_2885182) or DISC. OmniMap Anti-RB HRP RUO (Roche, 760-4311; RRID:AB_2811043) followed by fluorescently bound tyramides and neutralization by Discovery Inhibitor (RUO; Roche, 760-4840) in between staining rounds on a Roche Ventana Discovery ULTRA (Supporting Table S1). Nuclei were counterstained with DAPI (Thermo Scientific, 62248, Waltham, MA) at 1:1000 for 20 mins and coverslipped with Gelvatol.

B. Imaging

a. *Low resolution (LoRes) imaging.* Whole slide images (WSI) were captured via a Zeiss Axioscan Z.1 equipped with a Hitachi 16-bit 3-CCD color camera for brightfield and cooled 16-bit Hamamatsu CMOS monochrome camera for fluorescence acquisition with associated high-performance PC for automated WSI and both Colibri v7 LED and metal halide excitation sources. Acquisition resolution ranges from 0.111 μm/pixel for brightfield [40x, 0.95 numerical aperture objective] to 0.325 μm/pixel (20x, 0.8 numerical aperture objective) for fluorescence.
b. *High resolution (HiRes) imaging.* Using fiducial markers, identified iPAIRs/ai-iSYNs from LoRes WSI were mapped to the XY coordinates of the glass slide where, 0.06 μm/pixel fluorescence images were achieved with a 100x oil immersion, 1.46 NA objective using a Zeiss AxioImager M2 Motorized Microscope with Zen software for wide-field image acquisition with fluorescence and a AxioCam MRm Camera (Supporting Fig. S4). Using the 100x objective, Z-stacks through synapses were taken with

increments of 0.300 μm/step and Zen 2.3 software was used for image analysis. Fiducial markers were mapped when appropriate for locating portal vs lobular areas/boundary determinations.

C. Comparison of Qdot-linked vs. Tyramide-linked Staining Modalities

Control slides were generated from specimens using three different liver pieces (normal, inflamed, and cirrhotic). Staining was completed using either (A) streptavidin-biotin based amplification with tertiary detection via quantum dots on a LabVision 360 or (B) tyramide-based signal amplification with tertiary detection via traditional fluorophores on a Ventana DISCOVERY ULTRA. Four sets of serial sections were used whereby slide 1, 4, 7, and 10 (negative control) were stained with streptavidin-biotin based amplification and slides 2, 5, 8, 11 (negative control) were stained for tryamide-based signal amplification. Streptavidin-biotin based amplification is previously described in (4, 9). See above for full description of Tyramide-based signal amplification. WSI were generated and subjected to iPAIR detection as conducted in (4, 9). iPAIRs for all three liver tissues were combined for this analysis (n=3).

D. Surrogate Measures of Nuclear Flattening

Viewing lymphocyte ($CD45^{high}/MHCII^{any}$) nuclei as theoretical particles, nuclear features can be assessed and comparisons made between lobular lymphocytes within iPAIRs or as single unpaired lymphocytes. iPAIR evaluation incorporated the shortened ≤3 μm internuclear distance (Supporting Fig. S6). Nuclei were assessed for elongation (a surrogate of cell flattening) and compactness (a measure of roundness). Elongation is defined as the ratio of the nuclear Feret diameter (minimum to maximum perimeter points) for each lymphocyte while compactness is defined as the ratio of the calculated area to that of a circle having the same perimeter, whereby a perfectly round nucleus has a value of 1.0. To determine whether lobular iPAIR-engaged lymphocyte nuclei exhibited detectable shape changes on a LoRes WSI, n=1952 nuclei were randomly selected from lobular areas, split between iPAIR (n=998) and non-pair involvement (n=954), and compared.

E. Nanostring mRNA Expression Analysis with Biclustering Techniques

A set of 800 predefined genes (PanCancer Immune Profiling Panel with 30 additional genes based on their involvement in rejection, stellate cell function, and liver fibrosis) were evaluated (9). Raw data were normalized using the NanoStringNorm package9 (R using the geometric mean of the most stable genes [*MTMR14, CNOT10, MRPS5, EIF2B4, SF3A3, TLK2*]). Gene expression analysis was based on an identification algorithm using statistical modeling of the distribution and structure of quantitative spatial histopathology data via mathematical biclustering techniques, similar to known Bayesian BiClustering (55) methods for parameter inference (Supporting Fig. S8). To find similar co-expressing genes, we utilized the MCBiclust package in R (56) and the Nanostring Inflammatory Gene Panel (a subset of inflammatory genes related to related to antigen presentation, lymphocyte trafficking and activation) to define the initial mathematical correlations, and then determined which genes (from the entire Nanostring® Immune profiling panel, Supporting Table S2) most strongly associated with the correlation pattern. Gene correlation and expression levels were then evaluated for enrichment via Gene Ontology pathways [RRID:SCR_002811; (57, 58)]. Specimens were then ordered by correlation strength to the established pattern and summarized using statistical techniques.

SUPPORTING FIGURES

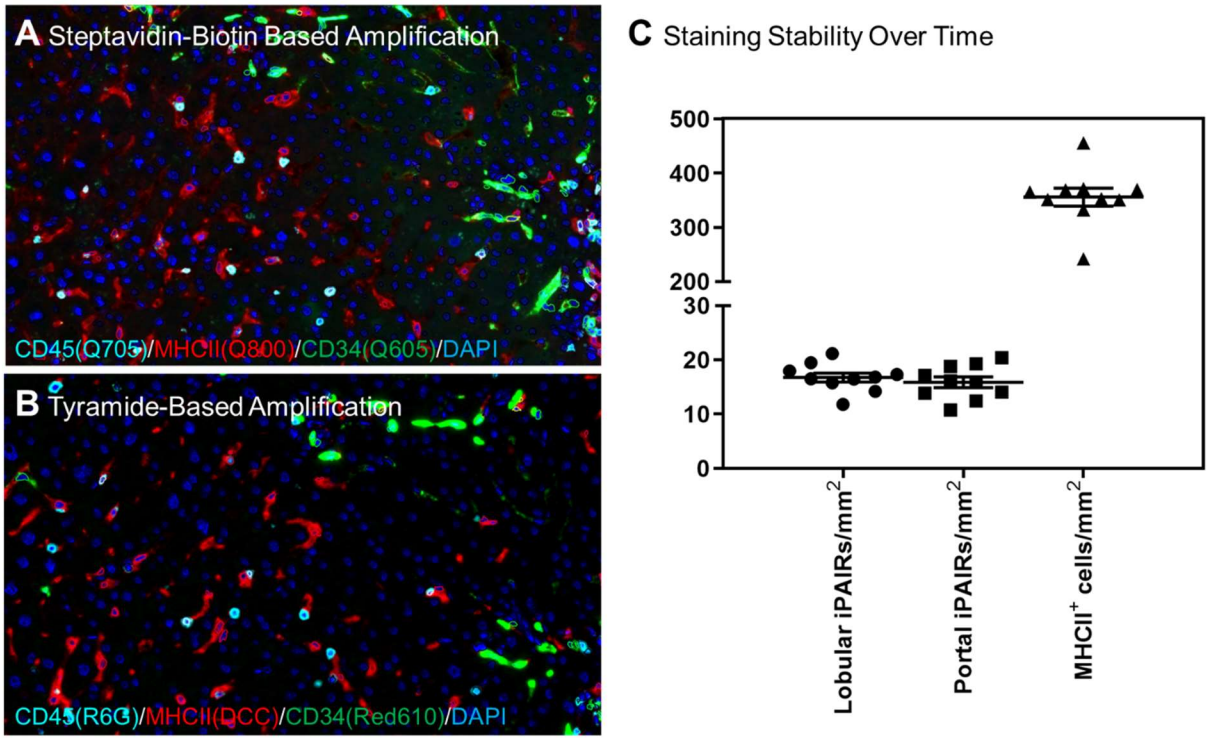

Supporting Figure S1. Similar iPAIR detection is achieved through use of two different staining modalities. To confirm that newer adaptations to our mIHC protocols did not affect staining results, control tissues were stained with both a protocol which uses Qdot-linked tertiary detection on a LabVision 360 Autostainer and a protocol using tyramide-linked tertiary detection on a Ventana Discovery Ultra. Representative images of mIHC for CD45 (cyan), MHCII (red), CD34 (green), and nuclei/DAPI (blue) using either (A) streptavidin-biotin based amplification with tertiary detection via quantum dots on a LabVision 360 or (B) tyramide-based signal amplification with tertiary detection via traditional fluorophores on a Ventana DISCOVERY ULTRA. (C) Stability of staining across 10 individual staining runs was assessed using tyramide-based amplification, followed WSI generation, and computer-assisted iPAIR calling and tissue tethered cytometry. Values were plotted as Mean±SEM where each dot represents single run and results were as follows: $MHCII^+$ cells/mm^2 (mean = 355.7; 95% CI 356±32.2), portal iPAIRs/mm^2 (mean = 15.88; 95% CI15.9 ±1.94), and lobular iPAIRs/mm^2 (mean = 16.75; 95% CI 16.75±1.61). This data supported our decision to modernize and streamline our mIHC workflow using the Ventana Discovery ULTRA and tyramide-linked tertiary antibodies.

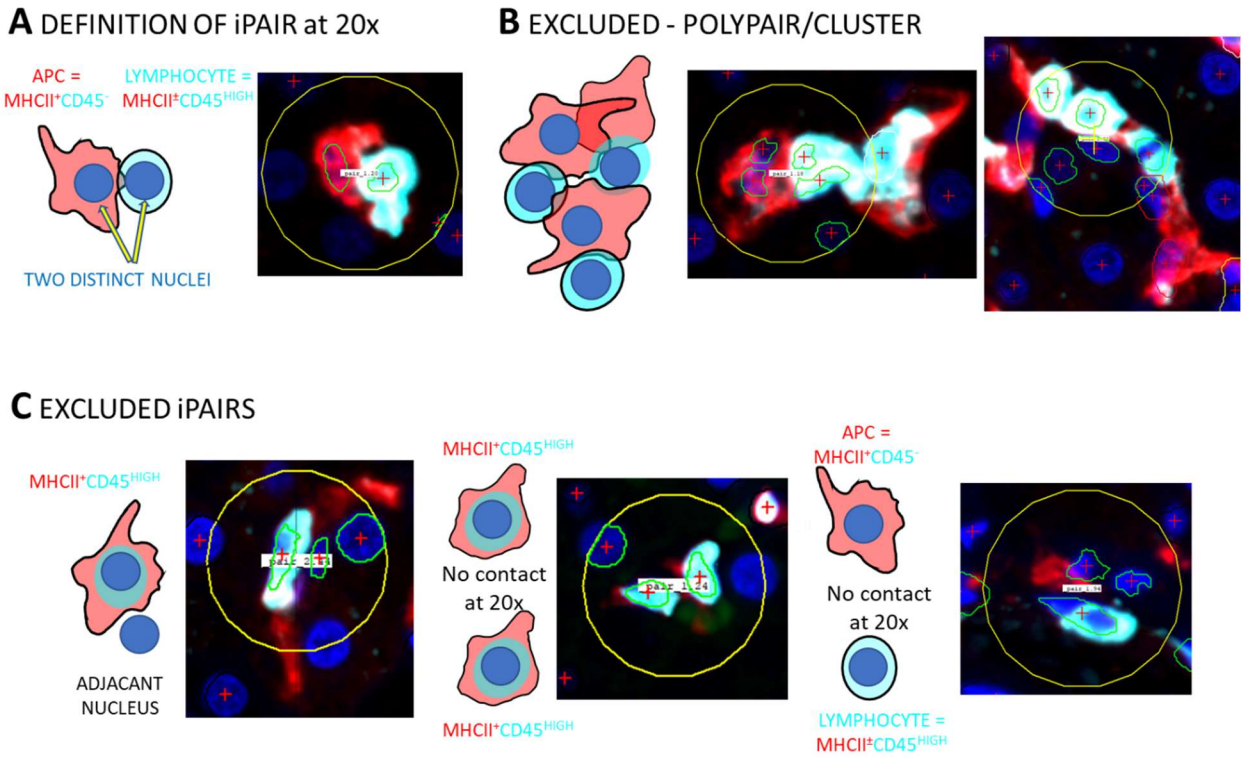

Supporting Figure S2. Representative Low-Resolution Images of Lobular iPAIRs classified by subjective observers. Cartoons and representative images of subcategories of lobular iPAIRs detected by NearCYTE (indicated by yellow circle). Identified nuclei are outlined in green. A) iPAIRs consisted of one APC ($MHCII^{+}$ cell/$CD45^{low/variable}$, interpreted as $CD45^{-}$) paired with one lymphocyte ($CD45^{high}$ cell with a single nucleus) where the nucleus of each cell could be clearly defined and appeared to be circular or oval shaped. Pairings were excluded from morphological analyses if they contained: (B) cells in polypairs/clusters characterized by more than two cells engaged in the iPAIR (e.g., two lymphocytes with a single APC, multiple lymphocytes with multiple APCs) (see also Supporting Fig. S4); or (C) very irregular nuclear shapes leading to improper nuclear segmentation into more than one cell (e.g., tiny subnuclear size signal with normal-sized cell, not shown); a single cell (or two nearby cells) that was double positive for CD45 and MHCII with a second unrelated ($MHCII^{-}$) nearby nucleus (left); possibly two cells near each other but with no apparent cytoplasmic interaction of the APC and the lymphocyte (right).

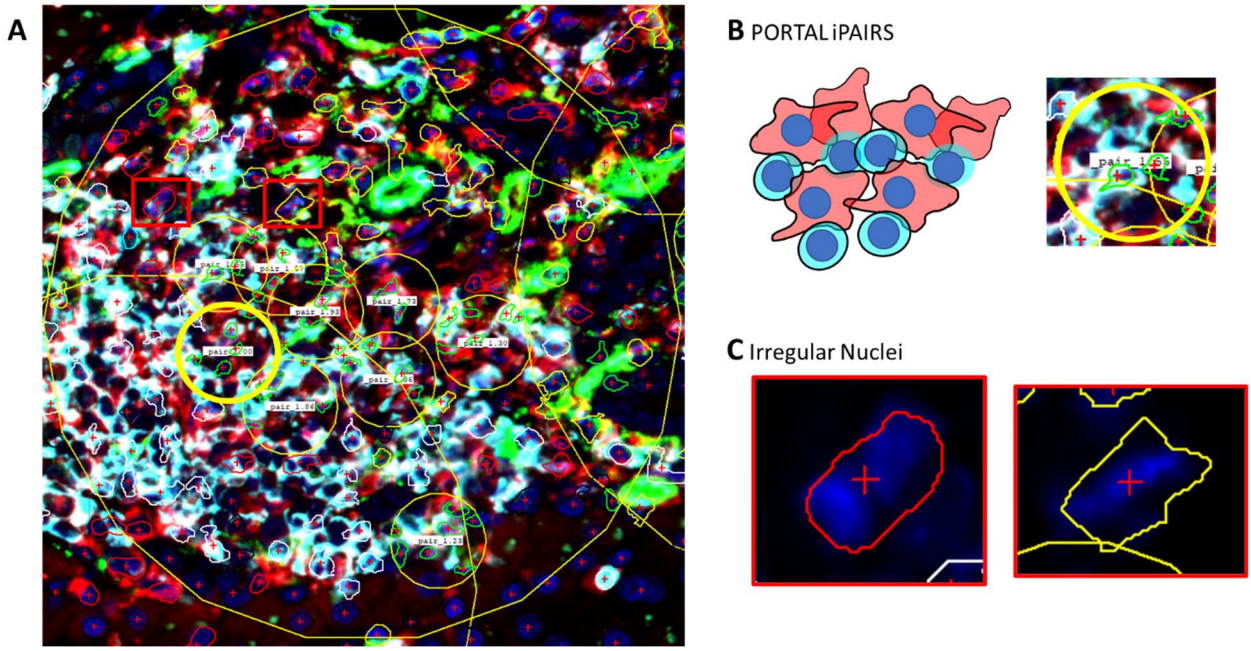

Supporting Figure S3. Portal iPAIRs are excluded from analysis. Although the human can recognize clusters of cells quite easily at a crude level, training a computer to classify individual cells meeting specific criteria requires features that allow for discrete cell classifications. (A) In large inflamed portal tracts (large circles), many inflammatory cells converge to a single location within the tissue. Although iPAIRs may be called within these inflamed regions (small yellow circles), the combination of improper segmentation coupled with closely packed and overlapping cytoplasm make confirmation of these cell-cell interactions challenging at low resolution. (B) Use of an automated classifier begins to breakdown due to the sheer number of cells, closely apposed cells, and results in overlapping and indistinguishable pairs. Representative defined iPAIR shown enlarged from thick yellow circle in A. (C) Nuclei fail to segment properly due to overlapping, irresolvable three-dimensional structures or lack of pixel shading between neighboring nuclei to distinguish between the two as seen in examples shown here enlargements of red boxes in A.

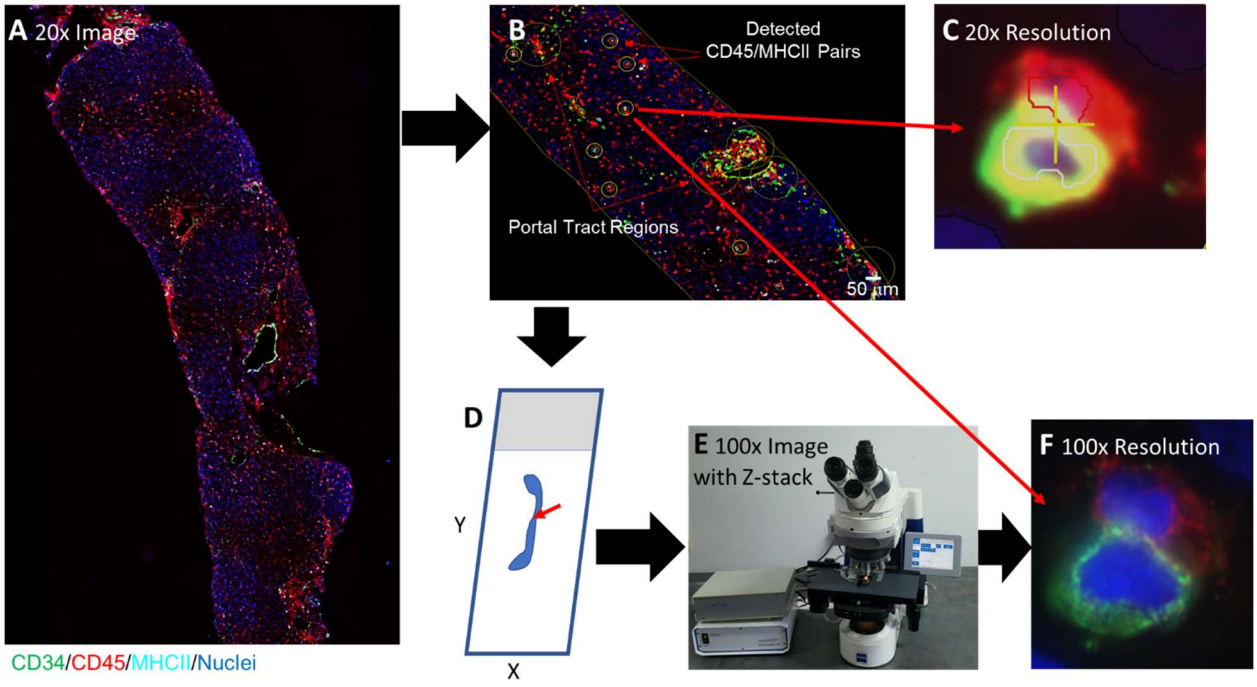

Supporting Figure S4. Fiducial Mapping of iPAIRs/ai-iSYNs identified on LoRes (0.325 µm/pixel) WSI to the glass slide for HiRes (0.06 µm/pixel) imaging. A) A biopsy stained with markers of interest [in this example: CD34 (green), CD45 (red), MHCII (cyan), and Nuclei (blue)] are imaged with a 20x objective (NA = 0.8) on a Zeiss Axioscan Z.1 whole slide scanner. B-C) Resultant scans are subjected to classification for features of interest, in this case, immune pairings between CD45 (green) and MHCII (red) with nuclei shown in blue. Yellow indicates overlap of green and red. D) Coordinates in pixels on the image are then translated to X,Y coordinates on the physical glass slide. E-F) Coordinates can then be used to locate the feature of interest on an AxioImager M.1 microscope for further evaluation at high resolution. Note the dramatic difference in resolving power between the LoRes and HiRes images of the same synapse.

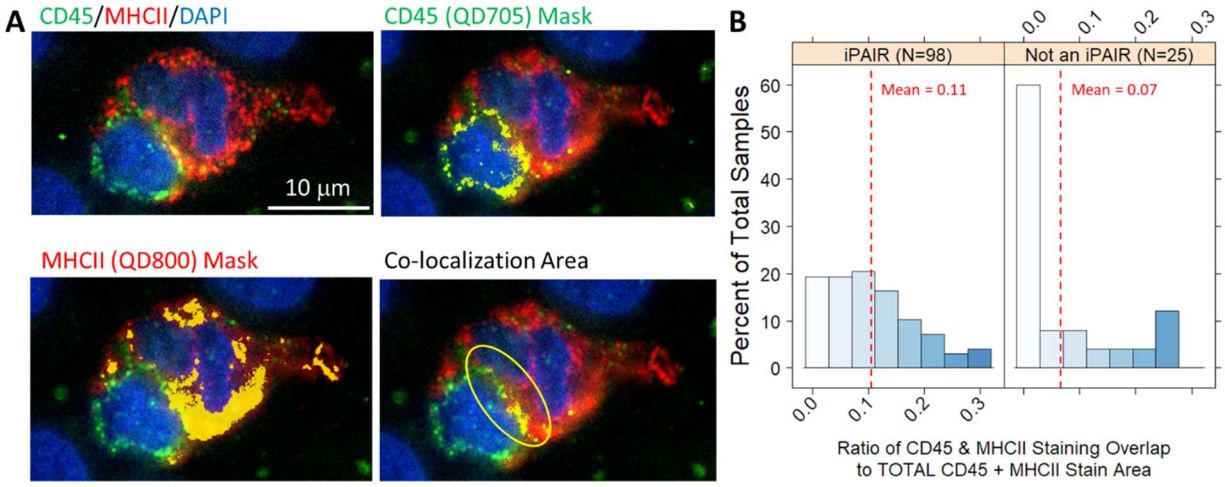

Supporting Figure S5. Cytoplasmic overlap between CD45^{high} cell and MHCII^{+} cell does not correlate with formation of a True Pair. (A) The upper left panel shows an iPAIR with a CD45^{+} lymphocyte (green) and a MHCII^{+} APC (red) with nuclei/DAPI (blue). The next two panels (upper right and lower left) show the individual masks created in Nearcyte, shown in yellow, generated for the two channels of interest: QD705 (CD45^{+}) and QD800 (MHCII^{+}). Co-localization area of the two channels can then be quantified by excluding all pixels that are not contained in both the CD45-QD705 channel and the MHCII-QD800 channel, as shown in the lower-right panel (oval, yellow). (B) Evaluation of co-localization area in iPAIRs on HiRes images by category and plotted as co-localization area (x-axis) by frequency of occurrence (y-axis). Red dashed line represents the mean of each group.

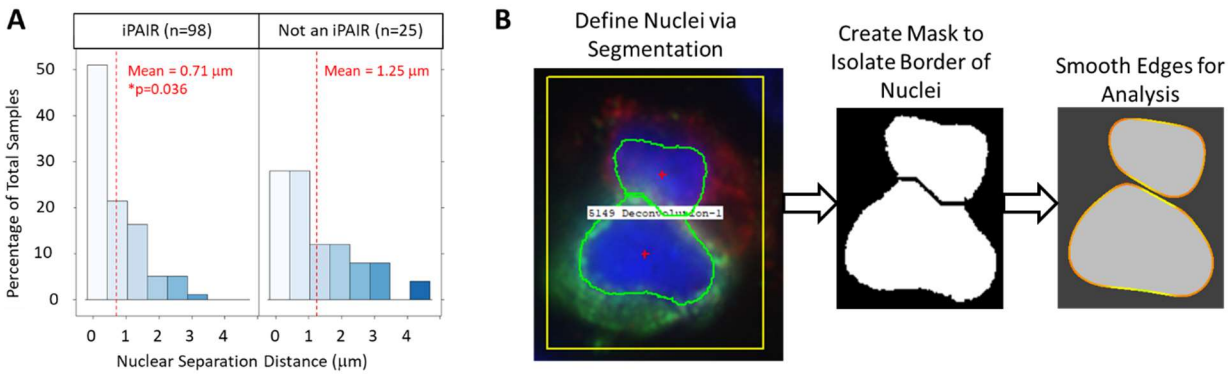

Supporting Figure S6. Implementation of a shorter nuclear distance and Level Set Smoothing in an enhanced classifier. (A) The distance between the lymphocyte and APC nucleus in each lobular iPAIR was evaluated at the closest approximation point (µm, x-axis) plotted by frequency of occurrence (y-axis). The red line is drawn at the mean distance for each category. iPAIRs in "Other" categories were excluded. The difference is statistically significant (p=0.036). (B) In our previous evaluation of biopsies, irregular spurs extending from suboptimal segmented nuclei were observed on occasional boundary segmentation overlays of images. Often these errors manifest as nuclear projections that remain after traditional segmentation, and thereby distort the morphology of the resultant nucleus. Therefore, level set smoothing was implemented to improve nuclear segmentation on LoRes images (59, 60). This approach minimizes or eliminates pixelation noise, where a smooth nuclear boundary would be interrupted by spurious image pixel intensity changes, resulting in a non-homogeneous shape. Level set smoothing for improved boundary detection of nuclear segmentation was applied prior to tissue-tethered cytometry.

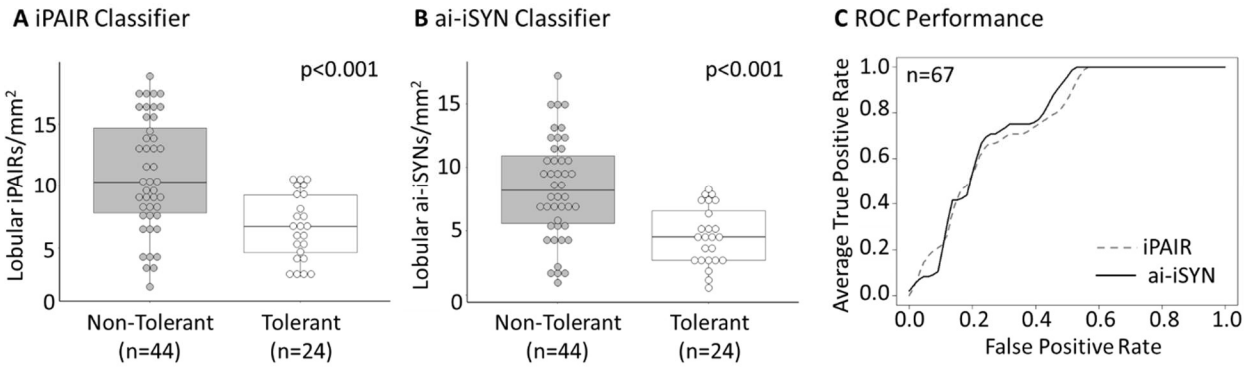

Supporting Figure S7. Comparison of iPAIR and ai-iSYN Classifier using baseline biopsies from iWITH. Identification and quantification of software-assisted detection of lobular immune pairings by the (A) iPAIR (original) classifier or by (B) the refined ai-iSYN classifier and grouped according to iWITH study endpoint: Non-Tolerant (gray, n=43), Tolerant (white, n=24). (C) Receiver operator characteristic curve for assessment of separation of tolerant patients vs. non-tolerant patients (n=67) based on the baseline biopsy. Comparison of the original iPAIR classifier (dashed line) vs. the refined ai-iSYN classifier (solid line) is shown. Use of deviance and log-likelihood tests showed no difference between the two classifiers.

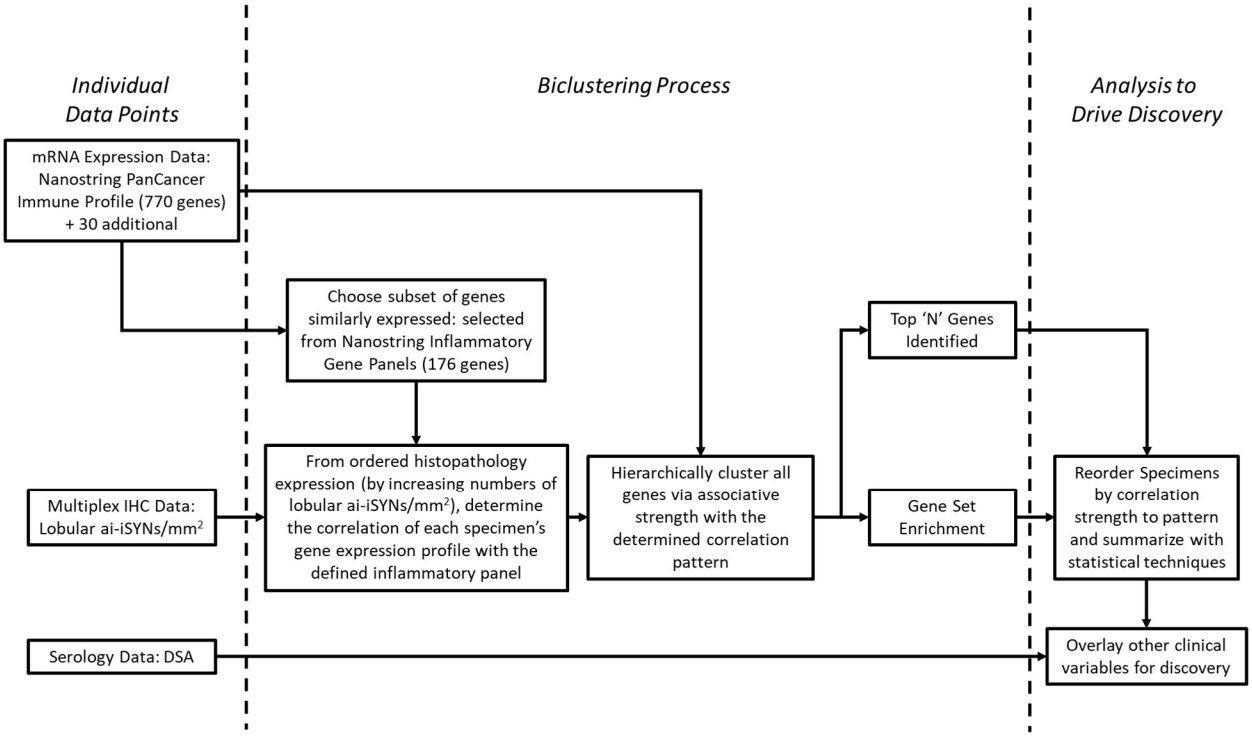

Supporting Figure S8. Description of Biclustering Method. Individual specimens from the iWITH clinical trial were subjected separately to mRNA expression analysis on the Nanostring nCounter platform for a set of 800 predefined genes (PanCancer Immune Profiling Panel with 30 additional genes based on their involvement in rejection, stellate cell function, and liver fibrosis). Biopsies were also subjected to mIHC analysis for the presence of ai-iSYNs/mm^2. Additional clinical parameters, like donor specific antigen (DSA) were gathered over the course of the clinical trial. Data was integrated using biclustering techniques. First, a subset of the mRNA expression data (176 genes from the Nanostring Inflammatory Gene panel) was chosen for integration with the number of lobular ai-iSYNs/mm^2 in specimens. The integration resulted in correlation of each specimen's gene expression profile in relation to the subset of inflammatory genes. The entire mRNA expression data set for each specimen was then clustered via associative strength based on each specimen's gene expression profile. From this supervised clustering, a top list of genes and gene set enrichment can be performed. To facilitate data discovery, specimens can be reordered by correlation strength to the gene expression profile and patterns can be identified using statistical methods such as principal component analysis. Additional clinical variables can then be overlay onto representations to drive questions about subsets of patients.

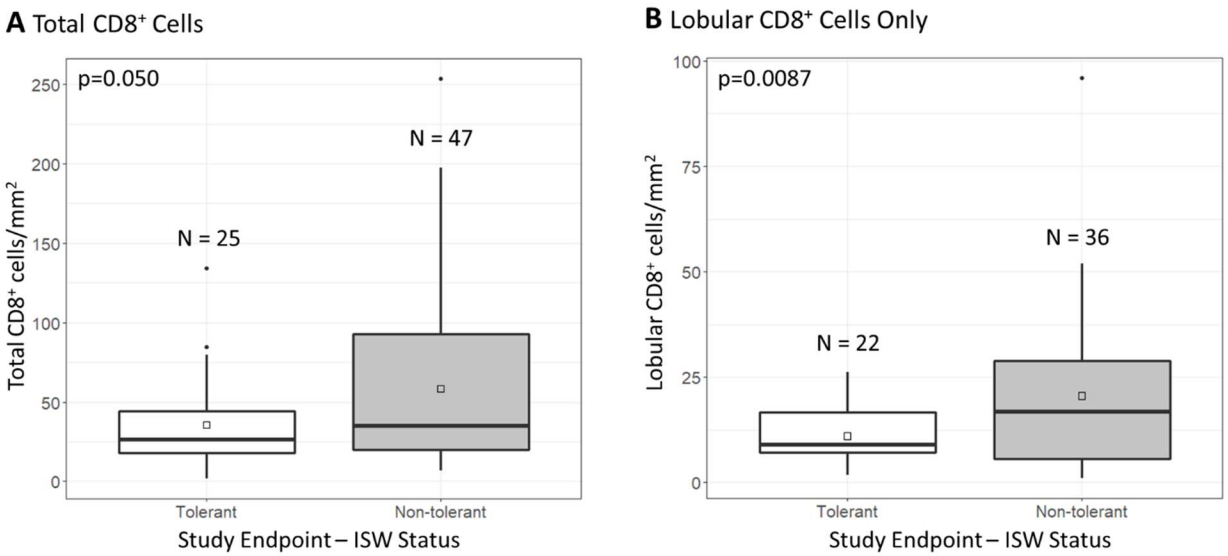

Supporting Figure S9. Comparison of use of Total CD8⁺ cells/mm² vs. Lobular CD8⁺ cells/mm². CD8⁺ cells/mm² were quantified after using improved nuclear segmentation, and fiducial mapping of CD8⁺ cells to lobular regions (based on MHCII clustering as previously described, Supporting Fig. S4). (A) Total CD8⁺ cells/mm² were elevated in non-tolerant (gray, n=47) and tolerant patients (white, n=25, Welch T-Test, p=0.050). Although significant, evaluation of lobular CD8⁺ cells/mm² showed highly significant differences between non-tolerant patients (gray, n=36) and tolerant patients (white, n=22, Welch T-Test, p=0.0087). P-values indicated are result of Welch's t-test.

SUPPLEMENTARY REFERENCES

55. Gu J, Liu JS. Bayesian biclustering of gene expression data. BMC Genomics 2008;9 Suppl 1:S4.

56. Bentham RB, Bryson K, Szabadkai G. MCbiclust: a novel algorithm to discover large-scale functionally related gene sets from massive transcriptomics data collections. Nucleic Acids Res 2017;45:8712-8730.

57. Ashburner M, Ball CA, Blake JA, Botstein D, Butler H, Cherry JM, Davis AP, et al. Gene ontology: tool for the unification of biology. The Gene Ontology Consortium. Nat Genet 2000;25:25-29.

58. Consortium GO. The Gene Ontology resource: enriching a GOld mine. Nucleic Acids Res 2021;49:D325-D334.

59. Wang Y, Songhe S, Tan Z, Wang D. Adaptive variational curve smoothing based on level set method. Journal of Computational Physics 2009;228:6333-6348.

60. Wang Z, Ma B, Zhu Y. Review of Level Set in Image Segmentation. Archives of Computational Methods in Engineering 2021;28:2429-2446.